

SEARCH FOR GAMMA-RAYS FROM THE UNUSUALLY BRIGHT GRB 130427A WITH THE HAWC GAMMA-RAY OBSERVATORY

A. U. ABEYSEKARA^{1,2}, R. ALFARO^{3,4}, C. ALVAREZ⁵, J. D. ÁLVAREZ⁶, R. ARCEO⁵, J. C. ARTEAGA-VELÁZQUEZ⁶,
H. A. AYALA SOLARES⁷, A. S. BARBER², B. M. BAUGHMAN⁴, N. BAUTISTA-ELIVAR⁸, S. Y. BENZVI^{9,10},
M. BONILLA ROSALES¹¹, J. BRAUN^{4,10}, K. S. CABALLERO-MORA¹², A. CARRAMINANA¹¹, M. CASTILLO¹³, U. COTTI⁶, J. COTZOMI¹³,
E. DE LA FUENTE¹⁴, C. DE LEÓN⁶, T. DEYOUNG¹, R. DIAZ HERNANDEZ¹¹, B. L. DINGUS¹⁵, M. A. DUVERNOIS¹⁰,
R. W. ELLSWORTH^{4,16}, D. W. FIORINO¹⁰, N. FRAIJA¹⁷, A. GALINDO¹¹, F. GARFIAS¹⁷, M. M. GONZÁLEZ^{4,17}, J. A. GOODMAN⁴,
M. GUSSERT¹⁸, Z. HAMPEL-ARIAS¹⁰, J. P. HARDING¹⁵, P. HÜNTEMAYER⁷, C. M. HUI⁷, A. IMRAN^{10,15}, A. IRIARTE¹⁷, P. KARN^{10,19},
D. KIEDA², G. J. KUNDE¹⁵, A. LARA²⁰, R. J. LAUER²¹, W. H. LEE¹⁷, D. LENNARZ²², H. LEÓN VARGAS³, J. T. LINNEMANN¹,
M. LONGO¹⁸, R. LUNA-GARCÍA²³, K. MALONE²⁴, A. MARINELLI³, S. S. MARINELLI¹, H. MARTINEZ¹², O. MARTINEZ¹³,
J. MARTÍNEZ-CASTRO²³, J. A. J. MATTHEWS²¹, E. MENDOZA TORRES¹¹, P. MIRANDA-ROMAGNOLI²⁵, E. MORENO¹³, M. MOSTAFÁ²⁴,
L. NELLEN²⁶, M. NEWBOLD², R. NORIEGA-PAPAQUI²⁵, T. O. OCEGUERA-BECERRA^{3,14}, B. PATRICELLI¹⁷, R. PELAYO²³, E.
G. PÉREZ-PÉREZ⁸, J. PRETZ²⁴, C. RIVIÈRE^{4,17}, D. ROSA-GONZÁLEZ¹¹, H. SALAZAR¹³, F. SALESA GREUS²⁴, A. SANDOVAL³,
M. SCHNEIDER²⁷, G. SINNIS¹⁵, A. J. SMITH⁴, K. SPARKS WOODLE²⁴, R. W. SPRINGER², I. TABOADA²², K. TOLLEFSON¹, I. TORRES¹¹,
T. N. UKWATTA^{1,15}, L. VILLASEÑOR⁶, T. WEISGARBER¹⁰, S. WESTERHOFF¹⁰, I. G. WISHER¹⁰, J. WOOD⁴, G. B. YODH¹⁹,
P. W. YOUNK¹⁵, D. ZABOROV²⁴, A. ZEPEDA¹², AND H. ZHOU⁷

(THE HAWC COLLABORATION)

- ¹ Department of Physics & Astronomy, Michigan State University, East Lansing, MI, USA
- ² Department of Physics & Astronomy, University of Utah, Salt Lake City, UT, USA
- ³ Instituto de Física, Universidad Nacional Autónoma de México, México D. F., Mexico
- ⁴ Department of Physics, University of Maryland, College Park, MD, USA
- ⁵ CEFyMAP, Universidad Autónoma de Chiapas, Tuxtla Gutiérrez, Chiapas, Mexico
- ⁶ Universidad Michoacana de San Nicolás de Hidalgo, Morelia, Michoacán, Mexico
- ⁷ Department of Physics, Michigan Technological University, Houghton, MI, USA
- ⁸ Universidad Politécnica de Pachuca, Municipio de Zempoala, Hidalgo, Mexico
- ⁹ Department of Physics & Astronomy, University of Rochester, Rochester, NY, USA
- ¹⁰ Wisconsin IceCube Particle Astrophysics Center (WIPAC) and Department of Physics, University of Wisconsin-Madison, Madison, WI, USA
- ¹¹ Instituto Nacional de Astrofísica, Óptica y Electrónica, Tonantzintla, Puebla, Mexico
- ¹² Centro de Investigación y de Estudios Avanzados del Instituto Politécnico Nacional, México D. F., Mexico
- ¹³ Facultad de Ciencias Físico Matemáticas, Benemérita Universidad Autónoma de Puebla, Ciudad Universitaria, Puebla, Mexico
- ¹⁴ Departamento de Física, Centro Universitario de Ciencias Exactas e Ingenierías, Universidad de Guadalajara, Guadalajara, Mexico
- ¹⁵ Physics Division, Los Alamos National Laboratory, Los Alamos, NM, USA
- ¹⁶ School of Physics, Astronomy & Computational Sciences, George Mason University, Fairfax, VA, USA
- ¹⁷ Instituto de Astronomía, Universidad Nacional Autónoma de México, México D. F., Mexico
- ¹⁸ Physics Department, Colorado State University, Fort Collins, CO, USA
- ¹⁹ Department of Physics & Astronomy, University of California, Irvine, Irvine, CA, USA
- ²⁰ Instituto de Geofísica, Universidad Nacional Autónoma de México, México D. F., Mexico
- ²¹ Department of Physics & Astronomy, University of New Mexico, Albuquerque, NM, USA
- ²² School of Physics and Center for Relativistic Astrophysics, Georgia Institute of Technology, Atlanta, GA, USA; dirk.lennarz@gatech.edu
- ²³ Centro de Investigación en Computación, Instituto Politécnico Nacional, México D. F., Mexico
- ²⁴ Department of Physics, Pennsylvania State University, University Park, PA, USA
- ²⁵ Universidad Autónoma del Estado de Hidalgo, Pachuca, Hidalgo, Mexico
- ²⁶ Instituto de Ciencias Nucleares, Universidad Nacional Autónoma de México, México D. F., Mexico
- ²⁷ Santa Cruz Institute for Particle Physics, University of California, Santa Cruz, Santa Cruz, CA, USA

Received 2014 October 5; accepted 2014 November 22; published 2015 February 11

ABSTRACT

The first limits on the prompt emission from the long gamma-ray burst (GRB) 130427A in the >100 GeV energy band are reported. GRB 130427A was the most powerful burst ever detected with a redshift $z \lesssim 0.5$ and featured the longest lasting emission above 100 MeV. The energy spectrum extends at least up to 95 GeV, clearly in the range observable by the High Altitude Water Cherenkov (HAWC) Gamma-Ray Observatory, a new extensive air shower detector currently under construction in central Mexico. The burst occurred under unfavorable observation conditions, low in the sky and when HAWC was running 10% of the final detector. Based on the observed light curve at MeV–GeV energies, eight different time periods have been searched for prompt and delayed emission from this GRB. In all cases, no statistically significant excess of counts has been found and upper limits have been placed. It is shown that a similar GRB close to zenith would be easily detected by the full HAWC detector, which will be completed soon. The detection rate of the full HAWC detector may be as high as one to two GRBs per year. A detection could provide important information regarding the high energy processes at work and the observation of a possible cut-off beyond the *Fermi* Large Area Telescope energy range could be the signature of gamma-ray absorption, either in the GRB or along the line of sight due to the extragalactic background light.

Key words: gamma-ray burst: individual (GRB 130427A) – gamma rays: general

1. INTRODUCTION

Gamma-ray bursts (GRBs) are the most luminous objects known (for a review, see, e.g., Gehrels et al. 2009) and although they have been studied since the late 1960s, their particle acceleration mechanisms are still poorly understood. The general picture is that a central engine, e.g., the core-collapse of a rapidly rotating star (collapsar; Woosley 1993) or the merger of two compact stellar remnants (Paczynski 1991; Narayan et al. 1992), creates a collimated relativistic outflow (fireball; for a review, see, e.g., Piran 1999). Internal shocks arise if relativistic jets with varied Lorentz factors collide in the outflow, and once the outflowing material interacts with the surrounding material, it creates external shocks. The main GRB lasts from 10^{-2} s to 10^3 s and most of the energy is emitted in the keV–MeV range. This prompt emission might arise from internal shocks or photospheric emission. It is followed by a multi-wavelength afterglow that lasts significantly longer and is generally attributed to the external shocks.

The Large Area Telescope (LAT) on board the *Fermi Gamma-Ray Space Telescope* (*Fermi*-LAT) recently found that the >100 MeV emission of GRBs not only starts later than the keV–MeV emission (e.g., reaching delays up to 40 s for GRB 090626), but is also temporally extended (Ackermann et al. 2013). In the afterglow synchrotron model, electrons accelerated by the external shock produce the temporally extended GeV emission via synchrotron radiation. However, in this scenario the maximum photon energy is limited (e.g., Piran & Nakar 2010). Hence, the observation of GeV photons at late times ($\gtrsim 100$ s) or TeV photons at late or early times are challenging synchrotron emission scenarios. An alternative scenario for non-thermal photons at GeV energies is inverse Compton radiation from the external shocks (e.g., Fan & Piran 2008).

Determining the highest energies and temporal evolution of GRB spectra thus has important implications for GRB physics and cannot be done by the LAT alone because the effective area is approximately constant above ≈ 10 GeV (<1 m²) and the photon flux decreases steeply with energy. Imaging Atmospheric Cherenkov Telescopes (IACTs) are sensitive to gamma rays at very-high energies (VHE; >100 GeV), however, only upper limits have been reported so far (Albert et al. 2007; Aharonian et al. 2009b; Acciari et al. 2011). One problem is that IACTs are pointed instruments that need to slew to the GRB position and will therefore in general miss the prompt and early afterglow phase (note, however, Aharonian et al. 2009a). The High Altitude Water Cherenkov (HAWC) observatory is a VHE gamma-ray extensive air shower (EAS) detector currently under construction. Its large instantaneous field of view (~ 2 sr or 16% of the sky), near 100% duty cycle and the lack of observational delays will allow observations during the prompt GRB phase.

VHE photons are attenuated due to interactions with the extragalactic background light (EBL) and are thus only possible for a very bright and nearby burst. GRB 130427A was an exceptionally bright and nearby GRB which made it a promising target for VHE observations. In this paper, the results of the analysis of HAWC data for this burst are reported.

2. GRB 130427A

The prompt phase of GRB 130427A triggered the *Fermi* Gamma-ray Burst Monitor (*Fermi*-GBM) at 07:47:06.42 UTC (Ackermann et al. 2014), denoted T_0 in the following. The *Swift* Burst Alert Telescope (BAT) did not trigger immediately, because triggering was de-activated during the slewing to a

pre-planned target (Maselli et al. 2014). GRB 130427A also triggered MAXI/GSC (Kawamuro et al. 2013), SPI-ACS/*INTEGRAL* (Pozanenko et al. 2013), Konus-*Wind* (Golenetskii et al. 2013), *AGILE* (Verrecchia et al. 2013) and *RHESSI* (Smith et al. 2013).

The BAT light curve can be divided into three main episodes. First, an initial pulse peaked at $T_0 + 0.5$ s with a smaller pulse at $T_0 + 1.1$ s. The second, main emission episode starts gradually at $T_0 + 2.2$ s with a sharp pulse at $T_0 + 5.4$ s and is followed by a complex structure of various emission peaks lasting a total of about 5 s. There are a few less intense pulses on top of the decay of the main episode, the last pulse peaking at about $T_0 + 26$ s. A third, much weaker episode starts at $T_0 + 120$ s, with two overlapping pulses peaking at $T_0 + 131$ s and $T_0 + 141$ s. The decaying emission was detectable until the end of the observations at $T_0 + 2021$ s. The central time interval, in which 90% of the prompt flux is detected (T_{90} , calculated over the first 1830 s of BAT data) is (276 ± 5) s.

At T_0 , the burst was well within the LAT field of view at a boresight of $47^\circ.3$ (Ackermann et al. 2014). The GBM initiated an Autonomous Repoint Request that started slewing at $T_0 + 33$ s and brought the burst within $20^\circ.1$ of the LAT boresight. The GBM light curve is similar to the BAT one, yielding a T_{90} of 138 s (von Kienlin 2013). The LAT Low Energy (LLE, >10 MeV) emission between $T_0 + 4$ s and $T_0 + 12$ s is roughly correlated with the GBM emission. At higher energies (HE, >100 MeV), there seems to be little correlation with the LLE or GBM emission, beyond an initial spike at T_0 . The GeV emission is delayed and between $T_0 + 11.5$ s and $T_0 + 33$ s an additional power-law component is required in the spectral fit.

Fermi-LAT detected temporally extended HE emission from this burst until it became occulted by the Earth after 715 s (Ackermann et al. 2014). The burst emerged from occultation at $T_0 + 3135$ s and remained detectable for about 20 hr (interrupted by further occultations). This unprecedented long HE emission easily surpasses the prominent GRB 940217, where the emission might have lasted more than 5000 s (Hurley et al. 1994). The GRB fluence is the highest ever detected by the GBM and LAT. Since the GRB redshift was found to be $z = 0.3399 \pm 0.0002$ (Levan et al. 2013; Xu et al. 2013; Flores et al. 2013), this yields, assuming a standard cosmology, an isotropic energy release of about 8.5×10^{53} erg, making it the most energetic GRB so far detected at a redshift $z < 0.5$ (Fan et al. 2013). This burst also featured the most energetic GRB photon ever detected (95.3 GeV or 128 GeV when corrected for the redshift) at $T_0 + 243$ s (Tam et al. 2013). This photon appears to be inconsistent with lepton synchrotron radiation in the standard afterglow model (Ackermann et al. 2014). Kouveliotou et al. (2013) find good agreement with the synchrotron model from optical to GeV energies and therefore suggest significant modifications to the relativistic shock physics.

3. THE HAWC GAMMA-RAY OBSERVATORY

HAWC is an EAS detector currently under construction at Sierra Negra, Mexico, at an altitude of 4100 m above sea level (Miguel Mostafa for the HAWC Collaboration 2013). It utilizes the water Cherenkov technique, where gamma rays are detected by measuring Cherenkov light from secondary particles in an EAS. HAWC has an order of magnitude better sensitivity, angular resolution and background rejection than its predecessor, the Milagro experiment (e.g., Atkins et al. 2003). Once completed, HAWC will consist of 300 steel tanks of 7.3 m diameter and 5.0 m height, containing a light-tight bladder

holding about 188,000 litres of filtered water. Each tank will have three 8" photomultiplier tubes (PMTs) and one 10" PMT on the bottom.

HAWC has two data acquisition (DAQ) systems. The main DAQ reads out full air-shower events by recording the time and charge of individual PMT pulses. The signal arrival time in different tanks permits reconstruction of the direction of the incident shower. The scaler DAQ counts the signals in each PMT in 10 ms windows, which is the finest possible granularity of a light curve. GRBs are detected by a statistical excess over the noise rate ("single particle technique"; Vernetto 2000). The DAQs complement each other, since they have different energy sensitivities (Abeysekara et al. 2012).

At T_0 , data were being collected by the scaler DAQ only using 29 operational tanks out of the 300 planned (called HAWC-30 and HAWC-300, respectively) and 115 deployed PMTs. The data of three PMTs are not considered in the following due to anomalous count rates.

3.1. Sensitivity

The zenith angle of GRB 130427A in the HAWC field of view was 57° and setting at T_0 . Seven hundred million gamma-ray air showers coming from the direction of GRB 130427A are simulated using CORSIKA version 7.4000 (Heck et al. 1998) with FLUKA version 2011.2b.6 (Böhlen et al. 2014; Ferrari et al. 2005). The energy range is 0.5 GeV–1 TeV, because lower energy showers produce no secondaries that reach the detector and absorption due to EBL cuts off the spectrum at energies beyond that. For comparison, one hundred million gamma-ray air showers randomly distributed on the sky down to a zenith angle of 60° and energies between 0.5 GeV and 10 TeV are simulated.

The detector response is simulated using a detailed detector description within GEANT4 version 10.0.1 (Agostinelli et al. 2003; Allison et al. 2006). It was originally developed for Milagro (Vasileiou 2008) and includes detailed descriptions of the geometrical and optical properties of the HAWC tanks and PMTs. The effective area of the scaler system is calculated by counting the hits in all PMTs (for details, see Abeysekara et al. 2012). Since each shower can create hits in multiple PMTs, the effective area is not restricted to the physical size of the detector. The biggest changes in the simulation compared to the previous publication are the inclusion of the fourth, central PMT and a more realistic simulation of the detector (see the discussion of systematic uncertainties below).

Figure 1 shows the effective area of the scaler system for HAWC-30 and the direction of GRB 130427A. For comparison, the effective area to bursts overhead for HAWC-30 and HAWC-300 is shown. The comparison between HAWC-30 and HAWC-300 shows that the effective area scales, as expected, linearly with the number of channels. The high zenith angle of GRB 130427A reduces the effective area by more than two orders of magnitude with respect to the zenith. Furthermore, the energy threshold is significantly worsened toward the horizon.

The width σ_μ of the summed scaler count distribution is larger than that of a Poissonian with mean μ because correlated sources of noise may produce two or more PMT signals, leading to multiple counting (Abeysekara et al. 2012). The widening is characterized by the Fano factor F : $\sigma_\mu^2 = F\mu$. Ten minutes of data are rebinned into 200 ms bins that make the count distribution of each channel Gaussian and then μ and σ_μ are calculated. The mean of the implied Fano factor for a day of data

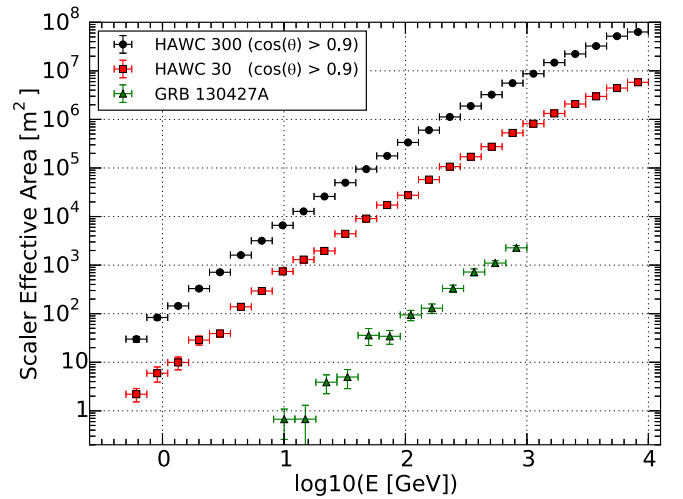


Figure 1. Effective area of the scaler system for HAWC-300 (black dots) and HAWC-30 (red boxes) for showers where the cosine of the zenith angle θ is larger than 0.9. The green triangles show the effective area for HAWC-30 for showers coming from the direction of GRB 130427A.

is 12.0. The analysis sensitivity is degraded by \sqrt{F} compared to a purely Poissonian background.

3.2. Systematic Uncertainties

3.2.1. Atmosphere

The atmosphere has a direct influence on shower development. To model the atmospheric conditions for GRB 130427A, data provided by the Global Data Assimilation System²⁸ (GDAS) from the closest grid point to the HAWC site are used. Using data from 2013-04-27T09:03:00 UTC, a profile of atmospheric depth is created following the procedure outlined in Pierre Auger Collaboration et al. (2012). The deviation to the profile measured three hours earlier is $<0.5\%$ at each altitude and therefore it can be concluded that the atmosphere was very stable during the observation period and any systematic uncertainty negligible.

For the simulation where the gamma-ray air showers are randomly distributed on the sky, a profile of atmospheric depth is created by averaging the GDAS data for the years 2011 and 2012 at each height. To investigate the systematic uncertainties, two additional profiles that represent the extreme, cumulative deviation from the average profile (above the altitude of HAWC) are selected, which should bracket the systematic error for the air shower development. Calculating the ratio of the effective areas for the two profiles and creating a weighted average over all energies, it was found that the difference is $\sim 8\%$. The effective area obtained from the average profile lies in the middle between the two profiles.

3.2.2. Water Quality

The propagation of Cherenkov light is influenced by the water in the tanks. The attenuation length has been measured at 405 nm using 1 m long water samples taken from 26 tanks and varies between 5 m and 16 m. Since all tanks contribute equally to the scaler effective area (e.g., two tanks with 50% more and less than the average counts give the same summed counts as two average tanks), the attenuation length can be averaged over all tanks. Taking into account the number of PMTs per tank considered in the analysis, this yields an attenuation

²⁸ <http://ready.arl.noaa.gov/gdas1.php>

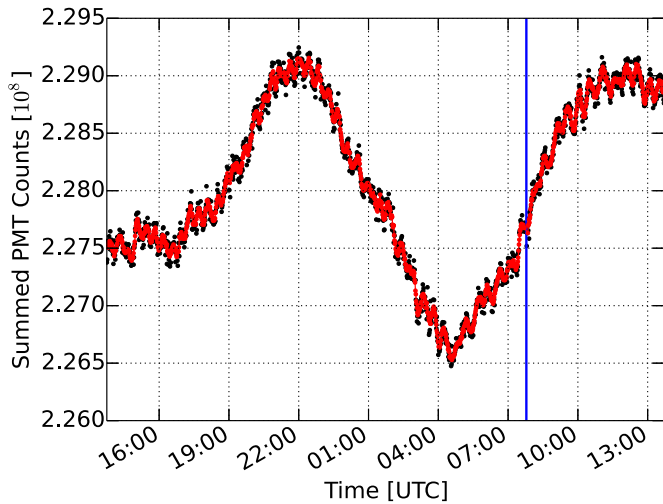


Figure 2. Black dots show the summed counts of all selected PMT channels (GRB 130427A trigger time shown as blue line) using a 60 s binning. The data are well described by the moving average (red line).

length of 10.4 m. Attenuation can be caused by absorption or scattering and these processes cannot be disentangled with current measurements. Absorption has a bigger impact on the scaler effective area, because a scattered photon may still be detected. The bladder holding the water is black on the inside to avoid reflection of photons. GEANT4 simulations are used to determine absorption and scattering parameters compatible with the measured attenuation length.

Vertically down-going muons provide well defined charge and timing signals in a HAWC tank and can be selected from raw data by applying appropriate charge and timing cuts. First studies indicate that the Monte Carlo describes the data well, assuming scattering properties comparable to those of clear seawater (Jonasz & Fournier 2011) and an absorption spectrum for water (Segelstein 1981) scaled so that the combination of absorption and scattering is compatible with the measured attenuation length at 405 nm. The same water properties have been used in the simulation where the gamma-ray air showers are randomly distributed on the sky.

The absorption spectrum between 300 nm and 550 nm varies strongly depending on impurities in the water. To characterize the systematic uncertainty, two simulations were done, with scattering either highly effective and causing most of the measured attenuation or highly ineffective and requiring more absorption. Calculating the ratio of the effective areas and creating a weighted average over all energies, it was found that the difference is 19%, which quantifies the total estimate for the systematic uncertainties, and the effective area given here for GRB 130427A is the average of these two extreme cases.

4. DATA ANALYSIS

4.1. Search Window Selection

A transient flux of gamma rays is identified by searching for an excess of the summed PMT counts over an expected background in a certain search window (SW). A first set of six partially overlapping SWs has been selected based on GRB Coordinates Network²⁹ (GCN) notices. The first window from $T_0 + 0$ s to $T_0 + 20$ s covers the first and second main emission periods seen by BAT and the second window ($T_0 - 5$ s to $T_0 + 55$ s) is an extension of that. The T_{90} reported by GBM motivated the

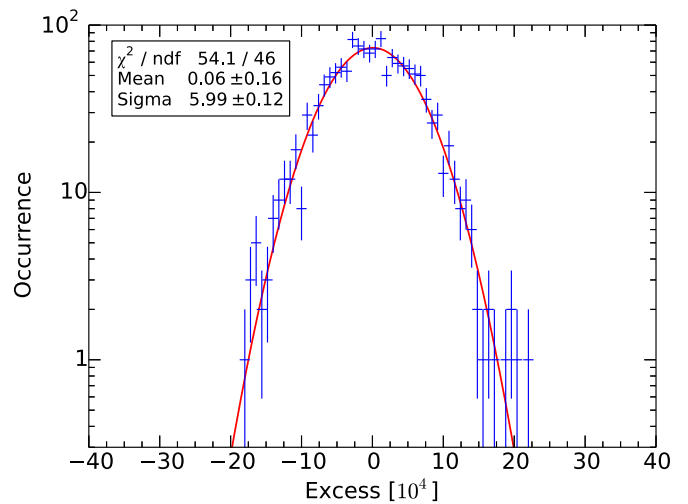


Figure 3. Histogram of the residuals between data and the moving average in the 60 s binning. A Gaussian fit (red line) describes the data well.

third time window ($T_0 - 5$ s to $T_0 + 145$ s). A time window from $T_0 + 120$ s to $T_0 + 300$ s was selected to cover the third emission period seen by BAT. All three BAT emission periods were combined in a time window from $T_0 - 10$ s to $T_0 + 290$ s. Additionally, a time window -10 s to 10 s around the time of the highest energy LAT photon was chosen. Preliminary results were reported in Lennarz & Taboada (2013). Besides the SWs, the data between -1200 s and $+1200$ s around the GRB trigger time were kept blind for future analysis.

A second set of SWs not previously reported is selected using intervals with hard power-law components in the GeV light curve. These are the window from $T_0 + 11.5$ s to $T_0 + 33$ s (index -1.66 , Ackermann et al. 2014) and the time window from $T_0 + 196$ s to $T_0 + 257$ s, where the power-law fit has a spectral index harder than -2 .

4.2. Background Estimation

The scaler data is rebinned to the different SW sizes. Figure 2 shows an example of the summed count rates of all selected PMT channels rebinned to 60 s (black points). The rates are influenced at the percent level by daily changes in the atmospheric pressure and temperature leading to differences in the shower development. A clear 12 hr modulation can be seen that corresponds to the local pressure cycle. This is long compared to the SWs and makes it unnecessary to correct the data for these environmental effects. The rates are also influenced by the temperature of the electronics, which has a ~ 27 minute cycle that can be seen in the data as well.

For each rebinning, a symmetric moving average (MA) is applied to each channel, where each point i is replaced by the average of the N points before and after (each having number of counts C):

$$\text{MA}(i) = \frac{1}{2N} \sum_{j=i-N; j \neq i}^{j=i+N} C(j). \quad (1)$$

The red line in Figure 2 shows the summed MAs. The differences to the data yield an excess distribution (see Figure 3), which shows no significant outliers and is well fit by a Gaussian (also true for the other binnings used). The analysis is more sensitive, the narrower this distribution is. An optimal sensitivity is obtained when N corresponds to an interval of 3 minutes on each side. For the 20 s and 21.5 s binning, $N = 9$ is used and

²⁹ <http://gcg.gsfc.nasa.gov>

Table 1
Results of the HAWC Analysis

	PMT Sum	BG ESt.	Excess	p -value	Upper Limit	Sensitivity	Fano Factor
	(10^4 counts)	(10^4 counts)	(10^4 counts)	(%)	(10^4 counts)	(10^4 counts)	
0–20 s	7593.0	7589.0	4.0	10.1	9.27	5.46	13
233–253 s	7590.6	7589.7	0.9	39.0	6.06	5.46	13
11.5–33 s	8161.3	8157.8	3.4	15.0	8.85	5.69	13
–5–55 s	22765.5	22765.4	0.2	48.9	10.15	10.46	16
196–257 s	23148.1	23148.2	–0.1	50.1	9.87	10.50	16
–5–145 s	56899.3	56927.5	–28.2	98.9	3.84	20.32	25
120–300 s	68308.5	68325.9	–17.4	90.3	9.15	23.57	28
–10–290 s	113826.7	113895.5	–68.8	99.6	10.96	52.08	77

Notes. For each search window, the sum of all PMT counts in that window is given together with the background estimation from the MA. From these two values the excess is calculated (using unrounded numbers). The p -value gives the probability that the background produces an equal or higher excess than the one observed (not accounting for the different trials). The event upper limits correspond to a 90% confidence level. Sensitivity is the corresponding average upper limit as defined in Feldman & Cousins (1998). The Fano factor is calculated as described in Section 4.2.

for 60 s and 61 s $N = 3$. Comparing the mean of the MA points to the width of the Gaussian fitted to the excess distribution implies Fano factors (see Table 1) close to the previously derived value. For all larger binnings, $N = 1$ is chosen. The Fano factor increases drastically in this case, reducing the sensitivity for the longest time window by more than a factor of two. Apparently, the MA is not optimal for longer time windows, possibly because of the cooling cycle on a similar timescale. This is a consideration for future enhancement of the analysis method.

Some points of the MA contain data from the SWs and would thus bias the background estimation. Those points are excluded and an unbiased background estimate for each SW is obtained by averaging the last and first point outside those times. Additionally, these points are also excluded from the excess distributions. The p -value of the excess in the SW, which is the probability that the observed or a higher excess is caused only by background, is calculated using the excess distribution.

5. RESULTS

Table 1 shows the results for each SW. All are consistent with the assumption of background only. Using Gaussian fits of the excess distributions, 90% confidence belts are constructed using the method described by Feldman & Cousins (1998) and upper limits on the number of excess events are derived. These upper limits are converted to integral flux upper limits between 0.5 GeV–1 TeV using the HAWC effective area for GRB 130427A.

Figure 4 visualizes the 11.5–33 s limit. The additional power law reported by LAT becomes significant after the GBM detected emission has faded and appears temporally distinct, suggesting that it might arise from a different emission region or mechanism (Ackermann et al. 2014). Assuming no intrinsic cut-off and modeling the absorption on the EBL according to the fiducial model in Gilmore et al. (2012), the combined best fit of GBM and LAT data is extrapolated to VHEs (dotted line). Under this assumption, the cut-off due to EBL happens just beyond the end of the LAT energy coverage. The scaler limit is calculated assuming the dotted line as the spectral shape. Since the scaler DAQ has no energy information, “quasi-differential” limits are calculated by restricting an E^{-2} spectrum to the energy ranges indicated by the limit bars. The green dashed–dotted lines show the sensitivity of the two HAWC DAQs for the full detector for

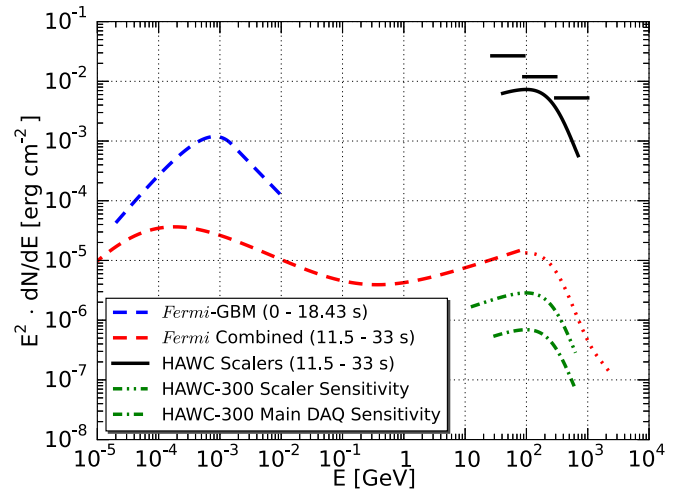


Figure 4. Dashed lines show the spectra fitted to the prompt GBM data (small energy range, blue) and the combined fit of GBM and LAT data when an additional power law is significant (larger energy range, red). The dotted continuation shows the effect of EBL absorption. Black lines show the scaler limit as an integral upper limit assuming the *Fermi* fit plus EBL absorption and as “quasi-differential” limits assuming E^{-2} . The green dashed–dotted lines show the sensitivity of the two HAWC DAQs for an overhead GRB. The limits are restricted to the energy range of 90% of the expected counts.

an overhead GRB. For the main DAQ, the line indicates the flux level which leads to a 50% probability for detecting a 5σ excess. For the scaler DAQ, the line shows the expected average upper limit. Since the Fano factor increases with the number of PMTs (and thereby reduces the sensitivity of the analysis), the scaler limit has been scaled by a factor of $\sqrt{3}$, assuming that the Fano factor increases by a factor of three in HAWC-300.

6. DISCUSSION

HAWC provides the first limits on the prompt emission of GRB 130427A in the VHE range. Due to the high zenith angle of the GRB and the incomplete HAWC detector, the limits are about two orders of magnitude higher than a simple extrapolation of the *Fermi* data. Had the GRB been observed overhead (cosine of zenith angle larger than 0.9), then it would have produced a 1.9σ effect in the HAWC-30 scaler DAQ. A similar GRB close to zenith would be easily detected by the full HAWC detector, which will be completed soon. In addition to

exceptional bursts like GRB 130427A, HAWC can also detect other GRBs with a rate as high as 1–2 GRBs per year (Taboada & Gilmore 2014).

Tam et al. (2013) showed that the LAT emission of GRB 130427 in five different time intervals fits well to a power law with an index of $\Gamma \sim -2$. Evidence was presented that after 3000 s a broken power-law model with break energy ~ 1 GeV, a soft low-energy component ($\Gamma \sim -2.6$), and a hard high-energy component ($\Gamma \sim -1.4$) is preferred at the 2.9σ level. The latter has properties consistent with synchrotron self-Compton (SSC) emission (Fan et al. 2013; Tam et al. 2013; Liu et al. 2013). A second analysis found that the GRB spectrum is well described by a power law at all times and a broken power law is not statistically required (Ackermann et al. 2014). A second broken power law described by Tam et al. (2013) between 138 s and 750 s was explained by Ackermann et al. (2014) as an effect of power laws with varying spectral indices over time. The VERITAS array has observed GRB 130427 ~ 20 hr after the onset of the burst (Aliu et al. 2014). The data disfavor the interpretation that the LAT emission originates from the SSC mechanism. Observations of GRB 130427A with HAWC-300 at a favorable zenith angle would have provided clear evidence for or against a possible SSC emission scenario.

HAWC can observe the prompt phase of GRBs that are typically not accessible to IACTs due to observational delays. A possible light curve could probe synchrotron and SSC scenarios and might reveal information on the interstellar density and magnetic field of the surrounding medium (e.g., Veres & Mészáros 2014). A spectrum at TeV energies could also probe possible hadronic-dominated scenarios, e.g., due to proton synchrotron emission (Böttcher & Dermer 1998). A joint main and scaler DAQ analysis could provide information on a possible cut-off beyond the LAT energy range (Abeysekara et al. 2012). Such a cut-off could be the signature of gamma ray absorption, either in the GRB (thus providing a probe of the bulk Lorentz factor) or along the line of sight (thus providing a probe of the EBL), or may also indicate the maximum particle energy produced by the GRB.

We acknowledge the support from: the US National Science Foundation (NSF); the US Department of Energy Office of High-Energy Physics; the Laboratory Directed Research and Development (LDRD) program of Los Alamos National Laboratory; Consejo Nacional de Ciencia y Tecnología (CONACyT), Mexico (grants 55155, 105666, 122331, 132197); Red de Física de Altas Energías, Mexico; DGAPA-UNAM (grants IG100414-3, IN108713, IN121309, IN115409, IN113612); VIEP-BUAP (grant 161-EXC-2011); the University of Wisconsin Alumni Research Foundation; the Institute of Geophysics, Planetary Physics, and Signatures at Los Alamos National Laboratory; the Luc Binette Foundation UNAM Postdoctoral Fellowship program.

REFERENCES

- Abeysekara, A. U., Aguilar, J. A., Aguilar, S., et al. 2012, *Aph*, **35**, 641
- Acciari, V. A., Aliu, E., Arlen, T., et al. 2011, *ApJ*, **743**, 62
- Ackermann, M., Ajello, M., Asano, K., et al. 2013, *ApJS*, **209**, 11
- Ackermann, M., Ajello, M., Asano, K., et al. 2014, *Sci*, **343**, 42
- Agostinelli, S., Allison, J., Amako, K., et al. 2003, *NIMPA*, **506**, 250
- Aharonian, F., Akhperjanian, A. G., Barres de Almeida, U., et al. 2009a, *ApJ*, **690**, 1068
- Aharonian, F., Akhperjanian, A. G., Barres de Almeida, U., et al. 2009b, *A&A*, **495**, 505
- Albert, J., Aliu, E., Anderhub, H., et al. 2007, *ApJ*, **667**, 358
- Aliu, E., Aune, T., Barnacka, A., et al. 2014, *ApJL*, **795**, L3
- Allison, J., Amako, K., Apostolakis, J., et al. 2006, *ITNS*, **53**, 270
- Atkins, R., Benbow, W., Berley, D., et al. 2003, *ApJ*, **595**, 803
- Böhlen, T. T., Cerutti, F., Chin, M. P. W., et al. 2014, The FLUKA Code: Developments and Challenges for High Energy and Medical Applications, Nuclear Data Sheets **120**, 211
- Böttcher, M., & Dermer, C. D. 1998, *ApJL*, **499**, L131
- Fan, Y.-Z., & Piran, T. 2008, *FrPhC*, **3**, 306
- Fan, Y.-Z., Tam, P. H. T., Zhang, F.-W., et al. 2013, *ApJ*, **776**, 95
- Feldman, G. J., & Cousins, R. D. 1998, *PhRvD*, **57**, 3873
- Ferrari, A., Sala, P. R., Fassò, A., & Ranft, J. 2005, FLUKA: A Multi-particle Transport Code (Program Version 2005) (Geneva: CERN)
- Flores, H., Covino, S., Xu, D., et al. 2013, *GCN*, **14491**, 1
- Gehrels, N., Ramirez-Ruiz, E., & Fox, D. B. 2009, *ARA&A*, **47**, 567
- Gilmore, R. C., Somerville, R. S., Primack, J. R., & Domínguez, A. 2012, *MNRAS*, **422**, 3189
- Golenetskii, S., Aptekar, R., Frederiks, D., et al. 2013, *GCN*, **14487**, 1
- Heck, D., Knapp, J., Capdevielle, J. N., Schatz, G., & Thouw, T. 1998, CORSIKA: A Monte Carlo Code to Simulate Extensive Air Showers (Karlsruhe, Germany: Forschungszentrum Karlsruhe GmbH)
- Hurley, K., Dingus, B. L., Mukherjee, R., et al. 1994, *Natur*, **372**, 652
- Jonasz, M., & Fournier, G. 2011, Light Scattering by Particles in Water: Theoretical and Experimental Foundations (Elsevier Science) (London: Academic Press)
- Kawamuro, T., Shidatsu, M., Nakahira, S., et al. 2013, *GCN*, **14462**, 1
- Kouveliotou, C., Granot, J., Racusin, J. L., et al. 2013, *ApJL*, **779**, L1
- Lennarz, D., & Taboada, I. 2013, *GCN*, **14549**, 1
- Levan, A. J., Cenko, S. B., Perley, D. A., & Tanvir, N. R. 2013, *GCN*, **14455**, 1
- Liu, R.-Y., Wang, X.-Y., & Wu, X.-F. 2013, *ApJL*, **773**, L20
- Maselli, A., Melandri, A., Nava, L., et al. 2014, *Sci*, **343**, 48
- Miguel Mostafa for the HAWC Collaboration. 2013, ICRC (arXiv:1310.7237)
- Narayan, R., Paczynski, B., & Piran, T. 1992, *ApJL*, **395**, L83
- Paczynski, B. 1991, *AcA*, **41**, 257
- Pierre Auger Collaboration, Abreu, P., Aglietta, M., et al. 2012, *Aph*, **35**, 591
- Piran, T. 1999, *PhR*, **314**, 575
- Piran, T., & Nakar, E. 2010, *ApJL*, **718**, L63
- Pozanenko, A., Minaev, P., & Volnova, A. 2013, *GCN*, **14484**, 1
- Segelstein, D. J. 1981, M. s. thesis, Univ. Missouri
- Smith, D. M., Csillaghy, A., Hurley, K., et al. 2013, *GCN*, **14590**, 1
- Taboada, I., & Gilmore, R. C. 2014, *NIMPA*, **742**, 276
- Tam, P.-H. T., Tang, Q.-W., Hou, S.-J., Liu, R.-Y., & Wang, X.-Y. 2013, *ApJL*, **771**, L13
- Vasileiou, V. 2008, ICRC, **3**, 1377
- Veres, P., & Mészáros, P. 2014, *ApJ*, **787**, 168
- Vernetto, S. 2000, *Aph*, **13**, 75
- Verrecchia, F., Pittori, C., Giuliani, A., et al. 2013, *GCN*, **14515**, 1
- von Kienlin, A. 2013, *GCN*, **14473**, 1
- Woosley, S. E. 1993, *ApJ*, **405**, 273
- Xu, D., de Ugarte Postigo, A., Schulze, S., et al. 2013, *GCN*, **14478**, 1